

Deformation of a nearly hemispherical conducting drop due to an electric field: Theory and experiment

L. T. Corson,¹ C. Tsakonas,² B. R. Duffy,¹ N. J. Mottram,¹ I. C. Sage,²
C. V. Brown,² and S. K. Wilson^{1,a)}

¹Department of Mathematics and Statistics, University of Strathclyde, 26 Richmond Street,
Glasgow G1 1XH, United Kingdom

²School of Science and Technology, Nottingham Trent University, Clifton Lane, Nottingham
NG11 8NS, United Kingdom

(Received 11 August 2014; accepted 15 November 2014; published online 19 December 2014)

We consider, both theoretically and experimentally, the deformation due to an electric field of a pinned nearly hemispherical static sessile drop of an ionic fluid with a high conductivity resting on the lower substrate of a parallel-plate capacitor. Using both numerical and asymptotic approaches, we find solutions to the coupled electrostatic and augmented Young–Laplace equations which agree very well with the experimental results. Our asymptotic solution for the drop interface extends previous work in two ways, namely, to drops that have zero-field contact angles that are not exactly $\pi/2$ and to higher order in the applied electric field, and provides useful predictive equations for the changes in the height, contact angle, and pressure as functions of the zero-field contact angle, drop radius, surface tension, and applied electric field. The asymptotic solution requires some numerical computations, and so a surprisingly accurate approximate analytical asymptotic solution is also obtained. © 2014 Author(s). All article content, except where otherwise noted, is licensed under a Creative Commons Attribution 3.0 Unported License. [<http://dx.doi.org/10.1063/1.4903223>]

I. INTRODUCTION

There is a growing technology-driven interest in using external influences to move or shape small quantities of fluids. The use of electrical, rather than mechanical, forces to achieve this manipulation is convenient, because the resulting devices contain no moving parts. The deformation or actuation of conducting drops can be achieved via a variety of techniques, including electrophoresis, electrowetting, and dielectrophoresis (DEP).

In electrophoresis, the drop may be suspended in air or in an insulating fluid medium. Transferring charge onto the drop enables it to be moved in a DC electric field using Coulombic forces.^{1–3}

In electrowetting on dielectric (EWOD), a conducting sessile drop rests on a substrate which consists of an electrode coated with a thin dielectric layer. The drop can be made to reduce its contact angle and hence to spread over the substrate through the application of a DC or an AC electric field between the drop and the electrode. Charge accumulates in the drop at the interface of the wetted area of the substrate, and equal and opposite charge accumulates on the electrode. The dielectric layer acts like a parallel-plate capacitor and the drop reduces its contact angle until the sum of the capacitive energy and the substrate and interfacial surface energies in the system is minimised.⁴ EWOD is becoming an established technology for drop manipulation and handling in digital microfluidics systems.^{5,6}

A related effect arises from DEP forces which occur when a dielectric medium is placed within a non-uniform electric field. In this situation, the non-uniformity of the electric field results in unequal Lorentz forces at the two poles of any dipole within the dielectric, leading to a resultant force. In liquid DEP, the dielectric contributions to the forces on a drop arise from the field-induced polarisation of

^{a)} Author to whom correspondence should be addressed. Electronic mail: s.k.wilson@strath.ac.uk



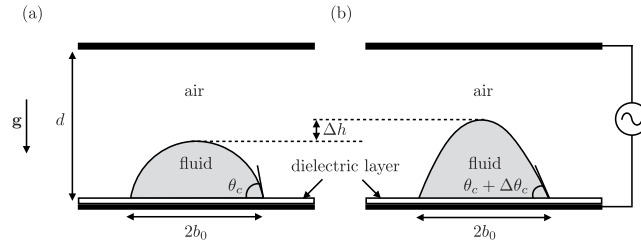


FIG. 1. Sketch of the geometry of a pinned sessile drop resting on the lower substrate of a parallel-plate capacitor. This substrate consists of an electrode coated with a thin dielectric layer. (a) No electric field applied. (b) An electric field applied across the capacitor deforms the drop, causing a change Δh in the height of the drop apex and a change $\Delta\theta_c$ in the contact angle.

bound charge within molecules and from the partial reorientation of any permanent molecular dipoles that are present.^{7,8} The non-uniform electric field creates a force on the drop interface which may be characterised by the Maxwell electric stress.⁹ The drop interface deforms to balance this force with those due to the interfacial surface tension and gravity. In fact, the EWOD and DEP forces are intimately related; for example, the standard EWOD drop spreading analysis may be re-cast as resulting from DEP forces arising at the droplet contact line, where the electric field is strongly non-uniform. Indeed, both effects arise from the Lorentz force which gives rise to Maxwell electric stresses at the interface, and are properly regarded as aspects of the same phenomenon.^{10,11} Like EWOD, liquid DEP has been exploited for moving drops and deforming drop interfaces, as well as to create forced wetting and spreading.^{12–14}

Forces can also arise on an electrically isolated neutral conducting drop when mobile free charges of opposite sign separate and polarise to opposite sides of the drop. Since this phenomenon involves free, rather than bound, charge it is normally described as “contactless” electrowetting.^{15,16}

The present study concerns the deformation due to an electric field of a drop of ionic fluid with a high conductivity. If a neutral drop is placed in a region of uniform electric field, any mobile charges arrange so that the electric field intensity is zero inside the drop. The electric field around the drop is distorted and becomes non-uniform since the drop interface is an equipotential and therefore the electric field lines must be normal to the interface. As in liquid DEP, this non-uniform electric field creates a force on the drop interface, causing it to deform. Taylor¹⁷ showed how this mechanism causes a free initially spherical drop to elongate and form a spheroid which is prolate in the direction of the applied external electric field.

The geometry used in our theoretical and experimental study is shown in Figure 1. A pinned sessile drop rests on the lower substrate of a parallel-plate capacitor. This substrate consists of an electrode coated with a thin dielectric layer. With no electric field applied, the drop adopts an equilibrium shape determined by the balance between the interfacial surface tension and gravity. An electric field applied across the capacitor deforms the drop, causing a change Δh in the height of the drop apex and a change $\Delta\theta_c$ in the contact angle.

Previous experimental work on the deformation of sessile conducting drops in this geometry has included work on soap bubbles,¹⁸ polymer drops,¹⁹ water drops in air,^{20–22} water drops immersed in dielectric oil,²³ and various alcohols in air.^{24–26} As well as different fluids, these experiments also considered different substrate treatments (untreated, hydrophilic, and hydrophobic), and therefore the zero-field contact angles of the drops varied greatly (specifically from 15° to 160°). As noted by Vancauwenberghe *et al.*,²⁷ these experiments show that, depending on the specific situation studied, the effect of applying an electric field may be either to increase or to decrease the contact angle of the drop.

Theoretical work in this geometry has tended to employ numerical techniques to solve the electrohydrodynamic equations for the electric field, the flow field, and the drop interface.^{18,19,28–30} For instance, Basaran and co-authors used a finite-element method to calculate the equilibrium shape and stability of perfectly conducting,¹⁸ and linearly²⁸ and non-linearly polarizable²⁹ dielectric axisymmetric sessile drops in an electric field. They considered drops with either a pinned contact line or a fixed contact angle both with and without the effect of gravity. Reznik *et al.*¹⁹ considered the evolution

of perfectly conducting axisymmetric drops with pinned contact lines in the Stokes-flow limit. More recently, Ferrera *et al.*³⁰ considered the evolution of perfectly conducting and leaky dielectric pendant drops with pinned contact lines. Both of these works used numerical techniques to calculate the drop evolution up to the point of drop break-up when jetting is initiated from the drop apex, and produced results that agreed well with the appropriate experiments.

Basaran and Scriven¹⁸ also performed an asymptotic analysis in the limit of a small electric field for initially hemispherical conducting drops when gravity is negligible. They showed that, when an electric field is applied, drops with fixed contact angles of $\pi/2$ evolve into a family of spheroidal shapes, while drops with fixed contact lines evolve into a family of conical shapes.

In the present work, we consider, both theoretically and experimentally, the deformation due to an electric field of a pinned nearly hemispherical static sessile drop of an ionic fluid with a high conductivity resting on the lower substrate of a parallel-plate capacitor. Using both numerical and asymptotic approaches, we find solutions to the coupled electrostatic and augmented Young–Laplace equations which agree very well with the experimental results. Our asymptotic solution for the drop interface extends that of Basaran and Scriven¹⁸ in two ways, namely, to drops that have zero-field contact angles that are not exactly $\pi/2$ and to higher order in the applied electric field, and provides useful predictive equations for the changes in the height, contact angle, and pressure as functions of the zero-field contact angle, drop radius, surface tension, and applied electric field. The asymptotic solution requires some numerical computations, and so a surprisingly accurate approximate analytical asymptotic solution is also obtained.

The remainder of this paper is organised as follows. In Sec. II, we describe the experimental setup and methods. Then, in Sec. III, we present the theoretical model for the equilibrium shape of the drop. In Sec. IV, we describe the numerical scheme used and verify the theoretical model by comparing the numerical and experimental results. Informed by these results, in Sec. V A and Sec. V B, we obtain the asymptotic solutions for the drop interface, contact angle, and pressure in the limit of small applied electric field and small deviations of the zero-field contact angle from $\pi/2$. These asymptotic solutions are compared with the experimental results in Sec. V C. Conclusions are drawn in Sec. VI.

II. EXPERIMENTAL SETUP

A sessile drop of the ionic fluid butyl methyl imidazolium tetrafluoroborate (BMIMTfB) rests on the lower substrate of a parallel-plate capacitor with gap d between the electrodes. The electrodes were formed from a continuous layer of transparent conductor, indium tin oxide (100 Ω /sq, 25 nm thickness, Praezisions Glas and Optik GmbH, Iserlohn, Germany), on borosilicate glass slides. The lower substrate consists of an electrode coated with a 1 μ m thick layer of the dielectric material SU8, as well as a commercial hydrophobic coating (Grangers International Ltd., Derbyshire, UK) to give contact angles close to $\pi/2$.

The ionic fluid BMIMTfB has a high conductivity σ of approximately 0.3 $\Omega^{-1} \text{ m}^{-1}$.³¹ It has a low vapour pressure and so shows negligible evaporation during the experiments.^{32–34} The surface tension γ of BMIMTfB was found from pendant drop measurements³⁵ (Drop Shape Analysis, A. Krüss Optronic GmbH, Hamburg, Germany) to be $40.9 \pm 0.5 \text{ mN m}^{-1}$ and its density ρ of 1120 kg m^{-3} was taken from the literature.³⁶ In this study, AC voltages (applied using a Trek model 609E-6 4 kV amplifier) at 1 kHz were used, and transparent electrodes enabled the drops to be viewed both from above and from the side during the experiments. Accurate values for the small changes in height in the range of 1–40 μ m were obtained using a 10 \times microscope objective with an extension tube which imaged the drop apex.

Figure 2 shows typical experimental images of the drop apex as the applied voltage is increased from 0 V to 2100 V. Images were recorded, contrast enhanced, thresholded, and the position of the drop apex was accurately obtained using standard imaging functions in MATLAB.³⁷ Experiments were conducted for 23 drops of various sizes with zero-field contact angles ranging from 88.9° to 98.4° (1.55 to 1.72 rad) and a range of cell gap to drop radius ratios from 2.26 to 7.07. In all experiments, the drop rapidly became static and the contact line of the drop was observed to be pinned by

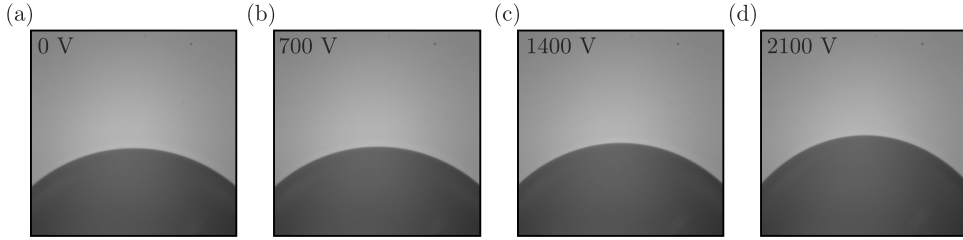


FIG. 2. Typical experimental images of the drop apex as the applied voltage is increased from 0 V to 2100 V.

surface roughness with no appreciable movement even at the highest voltages used. Experimental results for the change in the height of the drop apex Δh will be shown in Sec. IV.

III. THEORETICAL MODEL

In the theoretical model of the experiments described in Sec. II, an axisymmetric drop of a perfectly conducting fluid rests on the lower substrate of a parallel-plate capacitor surrounded by air, modelled as a perfect dielectric. Consistent with the experimental results, it is assumed that the drop is static and the contact line is pinned. We denote the constant drop base radius by b_0 and the zero-field contact angle by θ_c . At the top electrode, the electric potential is equal to the applied voltage V , and at the bottom electrode it is zero. The experiments used an AC field; however, since the charge relaxation time of the fluid is small compared to the reciprocal of the frequency of the field, it can be accurately represented by a DC field with the appropriate voltage.^{38,39} The electrodes are separated by a constant distance d , and we assume that the thickness of the dielectric layer on top of the lower electrode is negligible, so that the electric potential at the top of this layer can be assumed to be zero. This is a reasonable approximation given that the thickness of the dielectric layer (1 μm) is small compared with the other dimensions of our system: b_0 and d are of the order of millimetres.

We use spherical polar coordinates with their origin at the centre of the base of the drop, with r denoting the distance from the origin and θ the angle that the radial vector makes with the axis of symmetry, as shown in Figure 3. The drop interface is then defined as the zero level of the function $\eta = r - R(\theta)$, so that at any particular angle θ , the distance of the drop interface from the origin is $r = R(\theta)$.

The electric field $\mathbf{E} = -\nabla U$, where $U(r, \theta)$ is the electric potential, and the drop interface $r = R(\theta)$ are governed by Laplace's equation in the bulk and the normal stress balance, often termed the augmented Young–Laplace equation, on the drop interface:

$$\nabla^2 U = 0, \quad (1)$$

$$P - p_a - \rho g R \cos \theta + \mathbf{n} \cdot \boldsymbol{\tau} \cdot \mathbf{n} = \gamma \kappa. \quad (2)$$

Here, $P - \rho g R \cos \theta$ is the fluid pressure in which P is the constant modified (i.e., nonhydrostatic) pressure, p_a is the constant air pressure, ρ is the constant fluid density, $\boldsymbol{\tau}$ is the Maxwell stress in the air, γ is the constant surface tension, $\kappa = \nabla \cdot \mathbf{n}$ is twice the mean curvature, and the drop interface outward unit normal is

$$\mathbf{n} = \frac{\nabla \eta}{|\nabla \eta|} = \left(\frac{R}{\sqrt{R^2 + (R')^2}} \right) \hat{\mathbf{r}} - \left(\frac{R'}{\sqrt{R^2 + (R')^2}} \right) \hat{\boldsymbol{\theta}}. \quad (3)$$

The ij th component of the Maxwell stress $\boldsymbol{\tau}$ is given by

$$\tau_{ij} = \epsilon_0 \epsilon_2 \left(E_i E_j - \frac{1}{2} |\mathbf{E}|^2 \delta_{ij} \right), \quad (4)$$

where δ_{ij} is the Kronecker delta, ϵ_0 is the permittivity of free space, and $\epsilon_2 = \epsilon_{\text{air}}/\epsilon_0$ is the relative permittivity of the surrounding air; ϵ_2 is sufficiently close to one that we take it to be equal to unity.

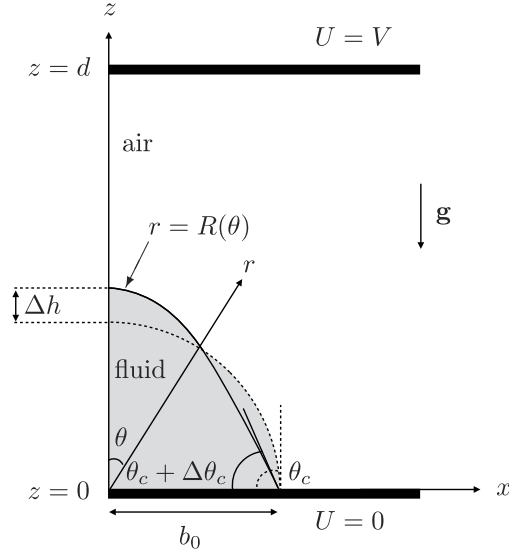


FIG. 3. Schematic diagram of the theoretical model. When an electric field is applied, the zero-field sessile drop (shown with a dashed line) deforms (shown with a solid line), causing a change Δh in the height of the drop apex and a change $\Delta\theta_c$ in the contact angle, while the contact line remains pinned.

Since the drop is assumed to be a perfectly conducting fluid, the electric potential inside the drop is constant, and is determined by the close proximity of the lower electrode which is fixed at $U = 0$. The boundary conditions for the electric potential at the two electrodes as well as at the surface of the drop are therefore

$$U(r, \pi/2) = 0, \quad (5)$$

$$U(r, \theta) = V \quad \text{on} \quad r \cos \theta = d, \quad (6)$$

$$U(R, \theta) = 0. \quad (7)$$

The conditions of a fixed contact line at $\theta = \pi/2$ and zero slope at $\theta = 0$ are given by

$$R(\pi/2) = b_0, \quad R'(0) = 0, \quad (8)$$

and the volume of the drop \mathcal{V} is given by

$$\mathcal{V} = \frac{2\pi}{3} \int_0^{\pi/2} R^3 \sin \theta \, d\theta, \quad (9)$$

which remains constant when the drop is deformed by the electric field.

The governing equations and boundary conditions are made dimensionless by writing

$$r = b_0 r^*, \quad R = b_0 R^*, \quad \kappa = \frac{1}{b_0} \kappa^*, \quad \mathcal{V} = \frac{2\pi b_0^3}{3} \mathcal{V}^*, \quad (10)$$

$$\mathbf{E} = \frac{V}{d} \mathbf{E}^*, \quad U = \frac{V b_0}{d} U^*, \quad P - p_a = \frac{\gamma}{b_0} P^*,$$

and we define a non-dimensional electric Bond number, a gravitational Bond number, and a scaled cell gap as

$$\delta^2 = \frac{\epsilon_0 \epsilon_2 V^2 b_0}{\gamma d^2}, \quad G = \frac{\rho g b_0^2}{\gamma}, \quad D = \frac{d}{b_0}, \quad (11)$$

respectively.

Then, with the stars dropped for clarity, the electric potential U and the drop interface R must satisfy

$$\nabla^2 U = \frac{1}{r^2} \frac{\partial}{\partial r} \left(r^2 \frac{\partial U}{\partial r} \right) + \frac{1}{r^2 \sin \theta} \frac{\partial}{\partial \theta} \left(\sin \theta \frac{\partial U}{\partial \theta} \right) = 0 \quad (12)$$

in the bulk, and

$$P - GR \cos \theta + \delta^2 \left(\mathbf{E} \cdot \mathbf{n} \right)^2 - \frac{1}{2} |\mathbf{E}|^2 = \kappa \quad (13)$$

on the drop interface $r = R$, subject to the boundary conditions

$$U(r, \pi/2) = 0, \quad (14)$$

$$U(r, \theta) = D \quad \text{on} \quad r \cos \theta = D, \quad (15)$$

$$U(R, \theta) = 0, \quad (16)$$

$$R(\pi/2) = 1, \quad (17)$$

$$R'(0) = 0, \quad (18)$$

and the volume constraint

$$\mathcal{V} = \int_0^{\pi/2} R^3 \sin \theta \, d\theta. \quad (19)$$

Once the drop interface and electric potential have been determined, the change in the height of the drop apex is given by

$$\Delta h = R(0) - R(0)|_{\delta^2=0}, \quad (20)$$

where $R(0)|_{\delta^2=0}$ is the zero-field height of the drop apex. The change in the contact angle is given by

$$\Delta \theta_c = \tan^{-1} \left(\frac{1}{R'(\pi/2)} \right) - \theta_c, \quad (21)$$

where θ_c is the zero-field contact angle, and the change in the modified pressure is given by

$$\Delta P = P - P|_{\delta^2=0}, \quad (22)$$

where $P|_{\delta^2=0}$ is the zero-field modified pressure.

IV. NUMERICAL RESULTS AND COMPARISON WITH EXPERIMENTAL RESULTS

The theoretical model derived in Sec. III was solved numerically using an iterative method implemented using COMSOL Multiphysics⁴⁰ and MATLAB³⁷ as follows: (i) a numerical solution of Laplace's equation (12) subject to (14)–(16) was found in a domain outside a drop in a rectangle of height D and width 20 which is sufficiently large to avoid boundary effects, where the drop interface R was taken to be the zero-field drop interface, with $P = 0$; (ii) the gradients on the drop interface of this solution for U were substituted into the normal stress balance (13) which was solved numerically subject to (17)–(19) to find an updated solution for the drop interface and pressure; (iii) this updated solution for the drop interface was then substituted into the numerical model for the electric potential and solved to give an updated solution for the potential U . Steps (ii) and (iii) were repeated until the solution for the drop interface had converged, specifically until

$$\max_{\theta \in [0, \frac{\pi}{2}]} \left| \frac{R_i(\theta) - R_{i-1}(\theta)}{R_{i-1}(\theta)} \right| \leq \xi, \quad (23)$$

where ξ is a tolerance and $R_i(\theta)$ is the solution for the drop interface at the i th iteration.

Numerical convergence was checked by considering drops with contact angles ranging from 85° to 95° (1.48 to 1.66 rad), all with the same radius (1 mm) and the same cell gap (5 mm) for three different tolerances: $\xi = 10^{-4}$, 10^{-6} , 10^{-8} . For each drop, the changes in the height of the drop apex, Δh , and the change in the contact angle, $\Delta \theta_c$, for all three tolerances agreed extremely well. All of the subsequent numerical results were obtained using the tolerance $\xi = 10^{-6}$.

Figure 4 shows typical numerical solutions for a drop with a zero-field contact angle of $\theta_c = \pi/2$, gravitational Bond number $G = 0.2$, and cell gap $D = 5$. Figure 4(a) shows how the drop interface changes as the electric Bond number δ^2 is increased; the drop apex rises towards the top electrode and, consistent with volume conservation, the contact angle decreases. This is shown in

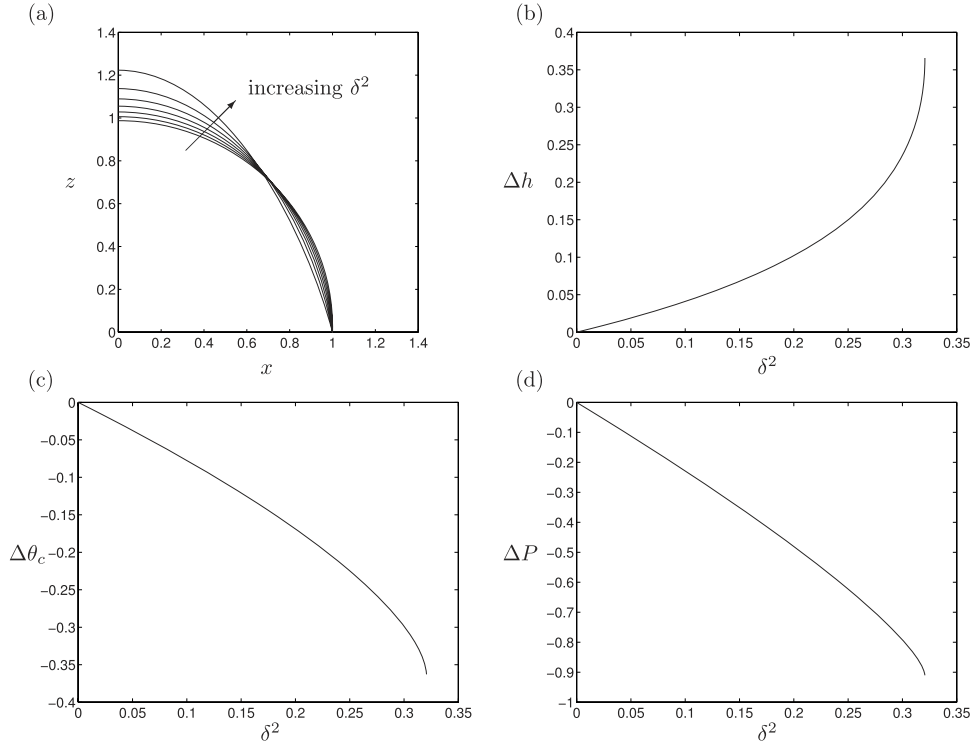


FIG. 4. Typical numerical solutions for a drop with a zero-field contact angle of $\theta_c = \pi/2$, gravitational Bond number $G = 0.2$, and cell gap $D = 5$; (a) drop interface with electric Bond number $\delta^2 = 0, 0.05, 0.1, 0.15, 0.2, 0.25, 0.3$; changes in (b) the height of the drop apex Δh , (c) the contact angle $\Delta\theta_c$, and (d) the modified pressure ΔP plotted as functions of the electric Bond number δ^2 .

Figures 4(b)–4(d), which show the changes in the height of the drop apex Δh , the contact angle $\Delta\theta_c$, and the modified pressure ΔP , respectively, plotted as functions of δ^2 . As δ^2 is increased, Δh increases from zero, while $\Delta\theta_c$ and ΔP decrease from zero. For smaller values of δ^2 , the variation is approximately linear in δ^2 and this behaviour is captured by the asymptotic solution presented subsequently in Sec. V. For larger values of δ^2 , the curves representing Δh , $\Delta\theta_c$, and ΔP have a fold bifurcation at a critical value of δ^2 ($\delta^2 \simeq 0.32$ in the particular case shown in Figure 4) beyond which no steady solution exists, as described by Basaran and Scriven.¹⁸

The numerically computed drop interface, equipotentials, and electric field vectors for the same drop with a zero-field contact angle of $\theta_c = \pi/2$, gravitational Bond number $G = 0.2$, cell gap $D = 5$, and electric Bond number $\delta^2 = 0.1$ are shown in Figure 5, which confirms that the equipotentials and electric field vectors lie perpendicular to each other, and that close to the drop the equipotentials lie parallel to the drop interface, while far from the drop they lie parallel to the electrodes.

Figure 6 shows the change in the height of the drop apex Δh , plotted as a function of the electric Bond number δ^2 for nine representative drops out of the 23 studied experimentally (shown with stars) along with the corresponding numerical solutions (shown with solid lines). For every experiment, the maximum applied voltage was between 2000 V and 2300 V, which corresponds to maximum electric Bond numbers in the range of $\delta^2 = 0.06$ to 0.18. These nine drops were chosen to illustrate the range of parameter values studied: the gravitational Bond number G which increases from panel (a)–(i), the cell gap D which decreases from panel (a)–(i), and the zero-field contact angle θ_c . As Figure 6 shows, there is very good agreement between the experimental results and the numerical solutions.

Figure 6 also shows numerical solutions using two additional simplifying assumptions: with gravity neglected, $G = 0$ (shown with dashed lines), and with the upper electrode infinitely far from the drop, $D \rightarrow \infty$ (shown with dashed-dotted lines). In particular, Figure 6 shows that, when D

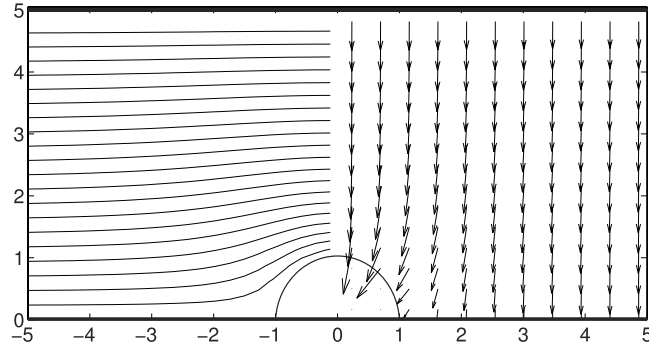


FIG. 5. Plot of the numerically computed drop interface, equipotentials (shown with solid lines), and electric field vectors (shown with arrows) for a drop with a zero-field contact angle of $\theta_c = \pi/2$, gravitational Bond number $G = 0.2$, cell gap $D = 5$, and electric Bond number $\delta^2 = 0.1$. The equipotentials are equally spaced between $U = 0$ and $U = D$.

is greater than approximately three, the assumption of an infinite cell gap is appropriate. Figure 6 also shows that, unsurprisingly, the assumption of negligible gravity is appropriate only when G is small, specifically when G is less than approximately 0.1. For many of the 23 experiments, $G < 0.1$ and $D > 3$, and so in these experiments the two additional simplifying assumptions of negligible gravity, $G = 0$, and an infinite cell gap, $D \rightarrow \infty$, are valid. In Sec. V we will construct an asymptotic solution of the theoretical model in the limit of small electric Bond numbers and small deviations of the zero-field contact angle θ_c from $\pi/2$ using these two additional simplifying assumptions.

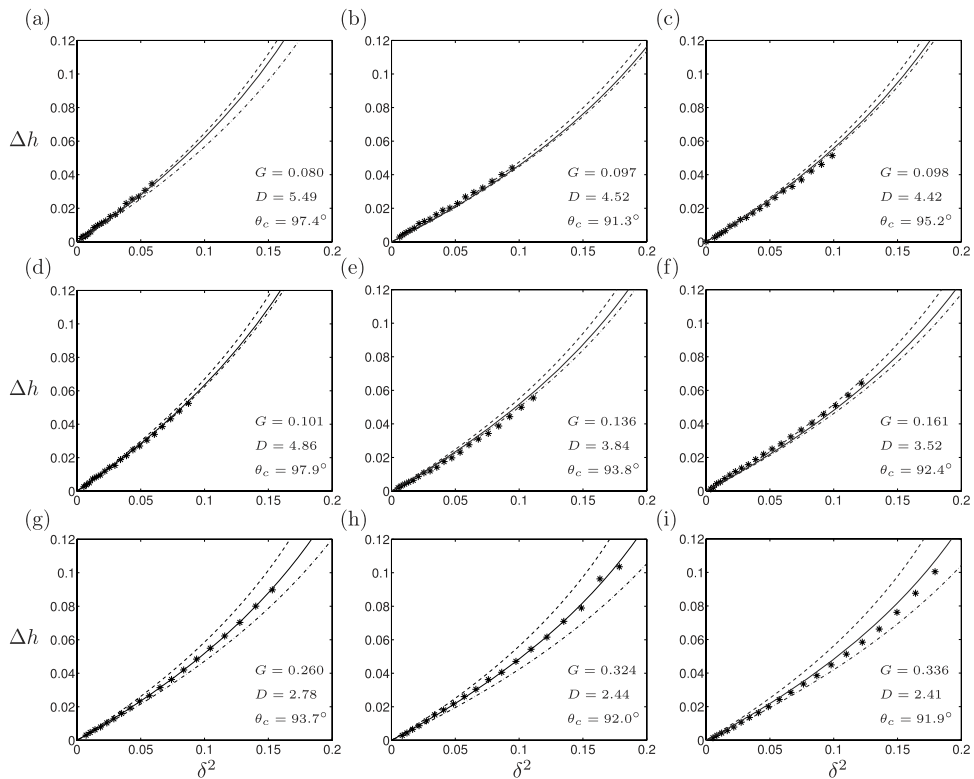


FIG. 6. The change in the height of the drop apex Δh plotted as a function of the electric Bond number δ^2 for nine representative drops (shown with stars) along with the corresponding numerical solutions (shown with solid lines). Also shown are numerical solutions using two additional simplifying assumptions: with gravity neglected, $G = 0$ (shown with dashed lines), and with the upper electrode infinitely far from the drop, $D \rightarrow \infty$ (shown with dashed-dotted lines).

V. ASYMPTOTIC SOLUTION AND COMPARISON WITH EXPERIMENTAL RESULTS

A. Asymptotic solution

Since all of the drops studied experimentally have zero-field contact angles θ_c close to $\pi/2$, and electric Bond numbers $\delta^2 < 0.2$, in this section we obtain the asymptotic solution of the theoretical model in the limit of small electric Bond numbers, $\delta^2 \rightarrow 0$, and zero-field contact angles which are close to $\pi/2$, so that $|\epsilon| \rightarrow 0$, where we have written $\theta_c = \pi/2 - \epsilon$. For simplicity, we use the two additional simplifying assumptions of negligible gravity, $G = 0$, and an infinite cell gap, $D \rightarrow \infty$, discussed previously in Sec. IV. Hence, the boundary condition on the upper electrode (15) is replaced by the far-field condition

$$U(r, \theta) \sim r \cos \theta \quad \text{as } r \rightarrow \infty. \quad (24)$$

The effect of a finite cell gap will be discussed in Sec. V D, while the effect of a fixed contact angle, rather than a pinned contact line, will be discussed in the Appendix. We note that the effect of gravity, $G \neq 0$, could, in principle, also be included; however, in this case, the zero-field drop interface is no longer a spherical cap and so would have to be found numerically.

When gravity is neglected, for any zero-field contact angle θ_c , the zero-field drop interface is a spherical cap which satisfies the quadratic equation

$$R^2 + \frac{2R \cos \theta}{\tan \theta_c} - 1 = 0, \quad (25)$$

with the appropriate solution

$$R = \left(1 + \frac{\cos^2 \theta}{\tan^2 \theta_c} \right)^{1/2} - \frac{\cos \theta}{\tan \theta_c}, \quad (26)$$

and hence the volume of the drop is given by

$$\mathcal{V} = \frac{2 + \cos^3 \theta_c - 3 \cos \theta_c}{2 \sin^3 \theta_c}, \quad (27)$$

which is a monotonically increasing function of θ_c . In the limit $\epsilon \rightarrow 0$, the zero-field drop interface can be written as

$$R = 1 - \epsilon \cos \theta + \frac{\epsilon^2}{2} \cos^2 \theta + O(\epsilon^3), \quad (28)$$

and the volume of the drop (27) becomes

$$\mathcal{V} = 1 - \frac{3}{2}\epsilon + \frac{3}{2}\epsilon^2 + O(\epsilon^3). \quad (29)$$

In the limit $\delta^2 \rightarrow 0$ and $\epsilon \rightarrow 0$, solutions for $R(\theta)$, $U(r, \theta)$, and P take the forms

$$\begin{aligned} R(\theta) = & 1 - \epsilon \cos \theta + \frac{\epsilon^2}{2} \cos^2 \theta + \delta^2 (R_{2,0}(\theta) + \epsilon R_{2,1}(\theta) + \epsilon^2 R_{2,2}(\theta)) \\ & + \delta^4 (R_{4,0}(\theta) + \epsilon R_{4,1}(\theta) + \epsilon^2 R_{4,2}(\theta)) + O(\delta^6, \epsilon^3), \end{aligned} \quad (30)$$

$$\begin{aligned} U(r, \theta) = & U_{0,0}(r, \theta) + \epsilon U_{0,1}(r, \theta) + \epsilon^2 U_{0,2}(r, \theta) + \delta^2 (U_{2,0}(r, \theta) + \epsilon U_{2,1}(r, \theta) + \epsilon^2 U_{2,2}(r, \theta)) \\ & + \delta^4 (U_{4,0}(r, \theta) + \epsilon U_{4,1}(r, \theta) + \epsilon^2 U_{4,2}(r, \theta)) + O(\delta^6, \epsilon^3), \end{aligned} \quad (31)$$

$$\begin{aligned} P = & P_{0,0} + \epsilon P_{0,1} + \epsilon^2 P_{0,2} + \delta^2 (P_{2,0} + \epsilon P_{2,1} + \epsilon^2 P_{2,2}) \\ & + \delta^4 (P_{4,0} + \epsilon P_{4,1} + \epsilon^2 P_{4,2}) + O(\delta^6, \epsilon^3), \end{aligned} \quad (32)$$

where the subscripts i, j correspond to the exponents of δ and ϵ , respectively.

Considering each order of the normal stress balance (13) in turn, we find at $O(1)$ that $P_{0,0} = 2$, while at $O(\epsilon)$, $P_{0,1} = 0$. At $O(\delta^2)$, we obtain

$$R''_{2,0}(\theta) + \cot \theta R'_{2,0}(\theta) + 2R_{2,0}(\theta) = -P_{2,0} - \frac{1}{2} \left[U_{0,0r}^2 \Big|_{r=1} - U_{0,0\theta}^2 \Big|_{r=1} \right], \quad (33)$$

where the subscripts r and θ denote derivatives in the radial and polar directions, respectively. Equation (33) must be solved subject to the boundary conditions $R_{2,0}(\pi/2) = 0$, $R'_{2,0}(0) = 0$, and the volume constraint

$$\int_0^{\pi/2} R_{2,0} \sin \theta \, d\theta = 0. \quad (34)$$

Substituting the asymptotic expansion (31) for U into (12) and boundary conditions (14)–(16), we find at $O(1)$ that

$$U_{0,0} = \left(r - \frac{1}{r^2} \right) \cos \theta. \quad (35)$$

Substituting this solution for $U_{0,0}$ into (33) leads to the solutions

$$R_{2,0}(\theta) = \frac{3}{8} \cos \theta (3 \cos \theta - 2) \quad (36)$$

and $P_{2,0} = -9/4$, recovering the leading order solution for a pinned contact line found by Basaran and Scriven.¹⁸

At $O(\epsilon^2)$, we find that $P_{0,2} = -1$, while at $O(\delta^2\epsilon)$, we obtain

$$R''_{2,1}(\theta) + \cot \theta R'_{2,1}(\theta) + 2R_{2,1}(\theta) = -P_{2,1} - 3 \cos \theta U_{0,1r}|_{r=1} - \frac{3}{2} \cos \theta (3 \cos^2 \theta + 2 \cos \theta + 3), \quad (37)$$

subject to the boundary conditions $R_{2,1}(\pi/2) = 0$, $R'_{2,1}(0) = 0$, and the volume constraint

$$\int_0^{\pi/2} R_{2,1} \sin \theta \, d\theta = \frac{1}{16}. \quad (38)$$

Furthermore, at $O(\delta^4)$, we obtain

$$\begin{aligned} R''_{4,0}(\theta) + \cot \theta R'_{4,0}(\theta) + 2R_{4,0}(\theta) \\ = -P_{4,0} - 3 \cos \theta U_{2,0r}|_{r=1} + \frac{9}{32} \cos \theta (3 \cos \theta - 2) (9 \cos^2 \theta + 2 \cos \theta + 6), \end{aligned} \quad (39)$$

subject to the boundary conditions $R_{4,0}(\pi/2) = 0$, $R'_{4,0}(0) = 0$, and the volume constraint

$$\int_0^{\pi/2} R_{4,0} \sin \theta \, d\theta = -\frac{3}{160}. \quad (40)$$

To find $R_{2,1}$ and $R_{4,0}$, we need first to find $U_{0,1}$ and $U_{2,0}$. At $O(\epsilon)$, the electric potential satisfies

$$\nabla^2 U_{0,1} = 0, \quad (41)$$

subject to the boundary and far-field conditions

$$U_{0,1}(r, \pi/2) = 0, \quad (42)$$

$$U_{0,1}(1, \theta) = 3 \cos^2 \theta, \quad (43)$$

$$U_{0,1}(r, \theta) \rightarrow 0 \quad \text{as } r \rightarrow \infty, \quad (44)$$

while at $O(\delta^2)$, the electric potential satisfies

$$\nabla^2 U_{2,0} = 0, \quad (45)$$

subject to the boundary and far-field conditions

$$U_{2,0}(r, \pi/2) = 0, \quad (46)$$

$$U_{2,0}(1, \theta) = -\frac{9}{8} \cos^2 \theta (3 \cos \theta - 2), \quad (47)$$

$$U_{2,0}(r, \theta) \rightarrow 0 \quad \text{as } r \rightarrow \infty. \quad (48)$$

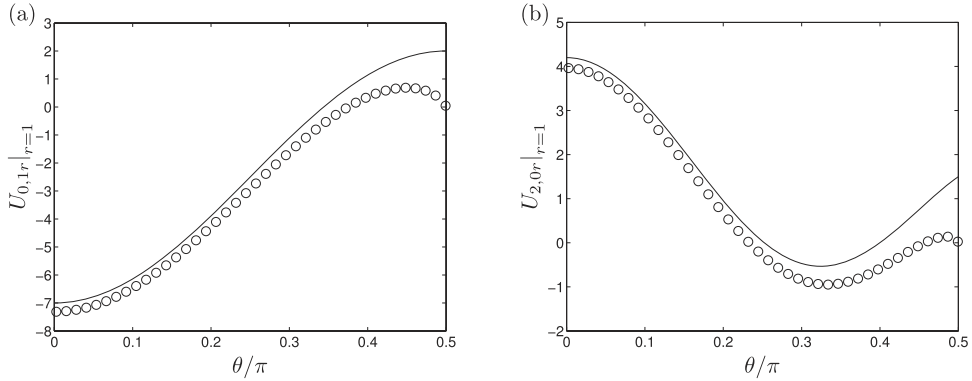


FIG. 7. The numerical solution (shown with circles) and separable part (shown with a solid line) for (a) $U_{0,1}|_{r=1}$ and (b) $U_{2,0}|_{r=1}$ plotted as functions of θ/π .

Unfortunately, we have been unable to find analytical solutions for $U_{0,1}$ and $U_{2,0}$. Therefore, we solved the systems of Eqs. (41)–(44) and (45)–(48) for $U_{0,1}$ and $U_{2,0}$ numerically using COMSOL Multiphysics,⁴⁰ in a domain consisting of a quarter circle of radius $r = 100$ with a quarter circle of radius $r = 1$ centred on the origin. The boundary at $r = 100$ is located sufficiently far from the origin to provide a good approximation to the infinite cell gap far-field conditions (44) and (48).

The circles in Figure 7(a) show the numerical solution for $U_{0,1r}$ on the interface $r = 1$ plotted as a function of θ/π . This solution is used to solve (37) numerically to obtain $P_{2,1}$ and $R_{2,1}(\theta)$. We find $P_{2,1} = 1.36437$ and the circles in Figure 8(a) show the solution for $R_{2,1}(\theta)$ plotted as a function of θ/π . Similarly, the circles in Figure 7(b) show the numerical solution for $U_{2,0r}$ on the interface $r = 1$ plotted as a function of θ/π which is used to solve (39) numerically to obtain $P_{4,0}$ and $R_{4,0}(\theta)$. We find $P_{4,0} = -0.77612$ and the circles in Figure 8(b) show the solution for $R_{4,0}(\theta)$ plotted as a function of θ/π . It is important to note that these calculations do not contain any parameters, and so need to be carried out only once to obtain the asymptotic solutions.

At the drop apex, we find that

$$R(0) = 1 - \epsilon + \frac{3}{8}\delta^2 + \frac{1}{2}\epsilon^2 - 0.96546\delta^2\epsilon + 0.54117\delta^4 + O(\epsilon^3, \delta^2\epsilon^2, \delta^4\epsilon, \delta^6), \quad (49)$$

and hence the change in the height of the drop apex Δh is given by

$$\Delta h = \frac{3}{8}\delta^2 - 0.96546\delta^2\epsilon + 0.54117\delta^4 + O(\delta^2\epsilon^2, \delta^4\epsilon, \delta^6). \quad (50)$$

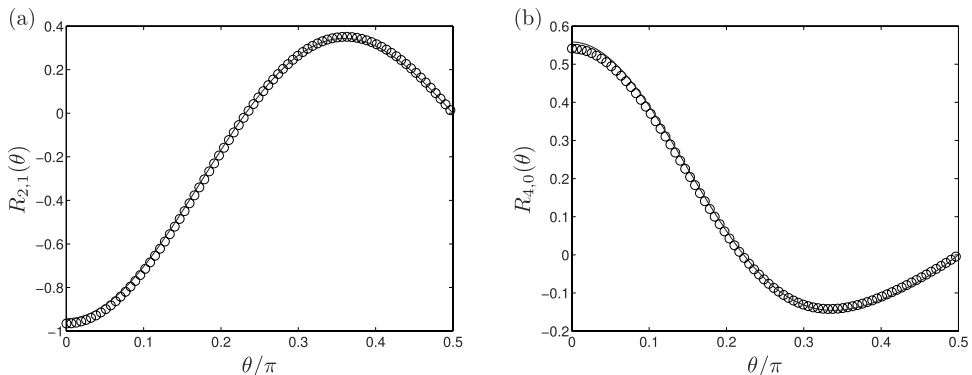


FIG. 8. The numerical solution (shown with circles) and the approximate solution (shown with a solid line) for (a) $R_{2,1}(\theta)$ and (b) $R_{4,0}(\theta)$ plotted as functions of θ/π .

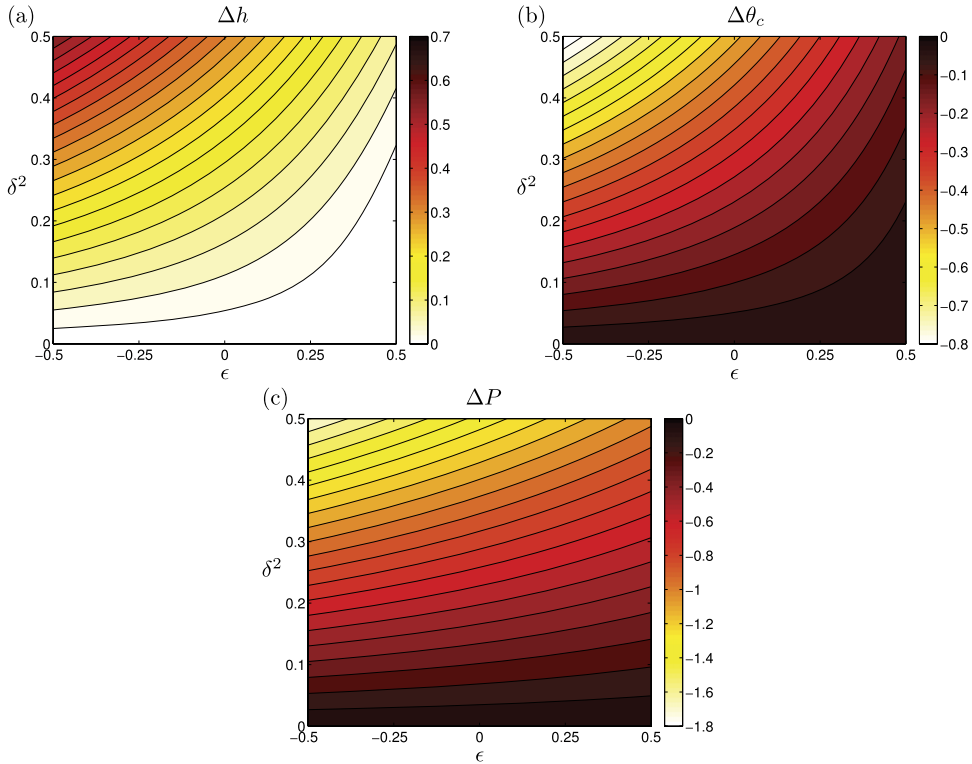


FIG. 9. The changes in (a) the height of the drop apex Δh given by (50), (b) the contact angle $\Delta\theta_c$ given by (51), and (c) the modified pressure ΔP given by (52), plotted as functions of δ^2 and ϵ .

Furthermore, the change in the contact angle $\Delta\theta_c$ is given by

$$\Delta\theta_c = -\frac{3}{4}\delta^2 + 1.36465\delta^2\epsilon - 0.43861\delta^4 + O(\delta^2\epsilon^2, \delta^4\epsilon, \delta^6), \quad (51)$$

and the change in the modified pressure ΔP is given by

$$\Delta P = -\frac{9}{4}\delta^2 + 1.36437\delta^2\epsilon - 0.77612\delta^4 + O(\delta^2\epsilon^2, \delta^4\epsilon, \delta^6). \quad (52)$$

The changes in the height of the drop apex Δh given by (50), the contact angle $\Delta\theta_c$ given by (51), and the modified pressure ΔP given by (52), are plotted as functions of δ^2 and ϵ in Figure 9. As ϵ increases, corresponding to a decrease in the zero-field contact angle, the magnitudes of Δh , $\Delta\theta_c$, and ΔP all decrease for a fixed value of δ^2 . Recall that the drop volume is a function of ϵ (cf. (29)) and as ϵ increases, the drop volume decreases; hence, it is not surprising that the magnitudes of the changes in the height and the contact angle are reduced for drops with smaller volumes.

B. Approximate asymptotic solution

As an alternative to employing numerical methods to find numerical solutions for the potentials $U_{0,1}$ and $U_{2,0}$, in this section we construct approximate analytical solutions which only partially satisfy the full system of equations. Since it is only the boundary condition at the lower substrate that precludes a separable solution to Laplace's equation, we consider approximate solutions of the form $U_{0,1} = U_{0,1}^s + U_{0,1}^r$ and $U_{2,0} = U_{2,0}^s + U_{2,0}^r$, where the solutions are split into separable and remainder parts. The separable parts are uniquely determined as a solution of Laplace's equation with all boundary conditions except for the one on the lower substrate. As we shall show, the separable parts turn out to be in surprisingly good agreement with the numerical solutions except for close to the lower substrate where we would naturally not expect good agreement since they do not

satisfy the boundary condition there. Hence, to construct approximate asymptotic solutions, we will neglect the remainder parts.

Specifically, we find that the separable parts are given by

$$U_{0,1}^s = \frac{1}{r} + \frac{3 \cos^2 \theta - 1}{r^3}, \quad (53)$$

$$U_{2,0}^s = \frac{3}{4r} - \frac{81 \cos \theta}{40 r^2} + \frac{3}{4} \left(\frac{3 \cos^2 \theta - 1}{r^3} \right) - \frac{27}{40} \left(\frac{\cos \theta (5 \cos^2 \theta - 3)}{r^4} \right). \quad (54)$$

Figure 7 compares the separable parts $U_{0,1r}^s$ and $U_{2,0r}^s$ on the interface $r = 1$ (shown with solid lines) with the numerical solution calculated previously in Sec. V A (shown with circles), plotted as a function of θ/π . The agreement between the solutions is surprisingly good except close to the lower substrate at $\theta = \pi/2$.

Substituting $U_{0,1} = U_{0,1}^s$ into (37) gives

$$R_{2,1}''(\theta) + \cot \theta R_{2,1}'(\theta) + 2R_{2,1}(\theta) = -P_{2,1} + \frac{3}{2} \cos \theta (15 \cos^2 \theta - 2 \cos \theta - 7), \quad (55)$$

subject to the boundary conditions $R_{2,1}(\pi/2) = 0$, $R_{2,1}'(0) = 0$, and the volume constraint (38), which has solutions

$$R_{2,1}(\theta) = -\frac{1}{4} \cos \theta (4 \ln(1 + \cos \theta) + 9 \cos^2 \theta - 3 \cos \theta - 5) \quad (56)$$

and $P_{2,1} = 1/2$. Figure 8(a) compares the approximate solution (56) (shown with a solid line) with the corresponding numerical solution for $R_{2,1}(\theta)$ (shown with circles). There is surprisingly good agreement between the two solutions even close to the lower substrate at $\theta = \pi/2$, even though the right-hand side of (55) is determined by the separable solution which does not satisfy the boundary condition there.

Substituting $U_{2,0} = U_{2,0}^s$ into (39) gives

$$\begin{aligned} R_{4,0}''(\theta) + \cot \theta R_{4,0}'(\theta) + 2R_{4,0}(\theta) \\ = -P_{4,0} - \frac{9}{160} \cos \theta (585 \cos^3 \theta - 300 \cos^2 \theta - 286 \cos \theta + 140), \end{aligned} \quad (57)$$

subject to the boundary conditions $R_{4,0}(\pi/2) = 0$, $R_{4,0}'(0) = 0$, and the volume constraint (40), which has solutions

$$R_{4,0}(\theta) = -\frac{3}{320} \cos \theta (80 \ln(1 + \cos \theta) - 195 \cos^3 \theta + 180 \cos^2 \theta - 156 \cos \theta + 56), \quad (58)$$

and $P_{4,0} = -57/40$. Figure 8(b) compares the approximate solution (58) (shown with a solid line) with the corresponding full numerical solution for $R_{4,0}(\theta)$ (shown with circles), and again shows that there is surprisingly good agreement between the two solutions.

From these approximate solutions, the corresponding approximate asymptotic solution for the change in the height of the drop apex Δh is given by

$$\begin{aligned} \Delta h &= \frac{3}{8} \delta^2 - \left(\frac{1}{4} + \ln 2 \right) \delta^2 \epsilon + \left(\frac{69}{64} - \frac{3}{4} \ln 2 \right) \delta^4 + O(\delta^2 \epsilon^2, \delta^4 \epsilon, \delta^6) \\ &= \frac{3}{8} \delta^2 - 0.94315 \delta^2 \epsilon + 0.55826 \delta^4 + O(\delta^2 \epsilon^2, \delta^4 \epsilon, \delta^6), \end{aligned} \quad (59)$$

the change in the contact angle $\Delta \theta_c$ is given by

$$\Delta \theta_c = -\frac{3}{4} \delta^2 + \frac{5}{4} \delta^2 \epsilon - \frac{21}{40} \delta^4 + O(\delta^2 \epsilon^2, \delta^4 \epsilon, \delta^6), \quad (60)$$

and the change in the modified pressure ΔP is given by

$$\Delta P = -\frac{9}{4} \delta^2 + \frac{1}{2} \delta^2 \epsilon - \frac{57}{40} \delta^4 + O(\delta^2 \epsilon^2, \delta^4 \epsilon, \delta^6). \quad (61)$$

Comparing the approximate asymptotic results (59)–(61) with the asymptotic results given by (50)–(52), we see that the approximate solutions for Δh and $\Delta \theta_c$ agree very well with the full

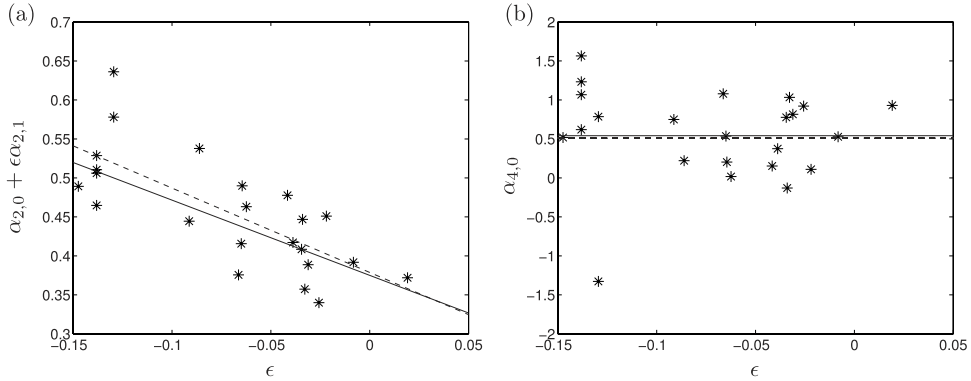


FIG. 10. The coefficients of δ^2 and δ^4 in (62), namely, (a) $\alpha_{2,0} + \epsilon\alpha_{2,1}$ and (b) $\alpha_{4,0}$, plotted as functions of ϵ for each experiment (shown with stars). The solid line shows the asymptotic solution in the case of an infinite cell gap given by (50), namely, $\alpha_{2,0} = 0.375$, $\alpha_{2,1} = -0.96546$, and $\alpha_{4,0} = 0.54117$. The dashed line shows the best-fit values from all 23 experiments, namely, $\alpha_{2,0} = 0.3788 \pm 0.0158$, $\alpha_{2,1} = -1.0825 \pm 0.2137$, and $\alpha_{4,0} = 0.5099 \pm 0.2218$.

solution, but the approximate solution for ΔP is in less good agreement. This discrepancy in ΔP , however, is to be expected since the approximate solution for the electric potential is not accurate close to the lower substrate at $\theta = \pi/2$, and the solution for the modified pressure is dependent on the entire drop profile. This method of obtaining an approximate analytical asymptotic solution could, in principle, be continued to higher orders, but we do not pursue this any further here.

C. Comparison of experimental results with asymptotic solutions

While, as we have seen, the numerical solutions of the theoretical model agree very well with the experimental results, it is of interest to see if the asymptotic solution in the limit of small electric Bond numbers and small deviations of the zero-field contact angle θ_c from $\pi/2$ obtained with the two additional simplifying assumptions of negligible gravity, $G = 0$, and an infinite cell gap, $D \rightarrow \infty$, also agrees with the experimental results. The asymptotic solution presented above shows that in the limit $\delta^2 \rightarrow 0$ and $\epsilon \rightarrow 0$, the change in the height of the drop apex is of the form

$$\Delta h = \delta^2(\alpha_{2,0} + \alpha_{2,1}\epsilon) + \delta^4\alpha_{4,0} + O(\delta^2\epsilon^2, \delta^4\epsilon, \delta^6). \quad (62)$$

To determine the values of the $\alpha_{i,j}$ s from the experimental results, we use multiple regression and, since the asymptotic solutions are useful approximations to the full solution only for sufficiently small values of δ^2 , we restrict ourselves to values of $\delta^2 < 0.1$.

Figure 10 shows the coefficients of δ^2 and δ^4 in (62), namely, $\alpha_{2,0} + \epsilon\alpha_{2,1}$ and $\alpha_{4,0}$, plotted as functions of ϵ for each experiment (shown with stars). The solid line shows the asymptotic solution in the case of an infinite cell gap given by (50), namely, $\alpha_{2,0} = 0.375$, $\alpha_{2,1} = -0.96546$, and $\alpha_{4,0} = 0.54117$, while the dashed line shows the best-fit values obtained from all 23 experiments, namely, $\alpha_{2,0} = 0.3788 \pm 0.0158$, $\alpha_{2,1} = -1.0825 \pm 0.2137$ with $R^2 = 0.55$, and $\alpha_{4,0} = 0.5099 \pm 0.2218$ with $R^2 = 0.003$. These experimentally determined values agree well with the asymptotic solution, although the latter value of R^2 is very low. This low value of R^2 is as a result of the large amount of scatter in the experimental values of $\alpha_{4,0}$, and, in particular, reflects the fact that the level of error in the experimental values is of the same size as δ^4 ; specifically, for small values of δ^2 , Δh is of the order of 10^{-2} which is of the same order as δ^4 .

D. Effect of a finite cell gap

The asymptotic solutions described in Subsections V A and V B are obtained with the two additional simplifying assumptions of negligible gravity and an infinite cell gap. The experiments, however, are, of course, conducted with a finite cell gap, and, as we have already seen, the infinite cell gap approximation is not appropriate for all of the experimental drops. In the case of a finite

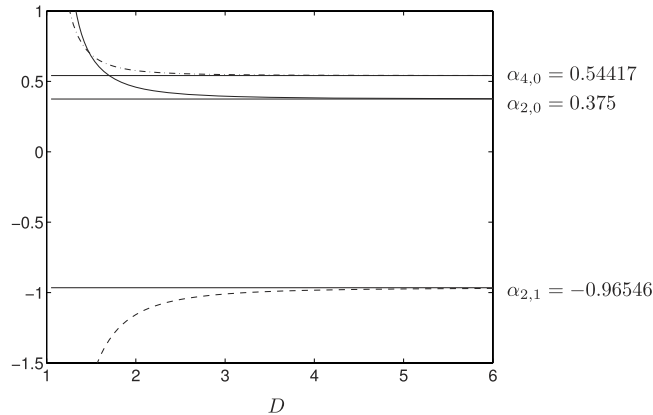


FIG. 11. The numerically calculated values of $\alpha_{2,0}$ (shown with a solid line), $\alpha_{2,1}$ (shown with a dashed line), and $\alpha_{4,0}$ (shown with a dashed-dotted line) plotted as functions of the cell gap D . The straight lines show their constant values in the case of an infinite cell gap given by (50).

gap, the boundary condition for the electric potential at the top electrode is given by (15) and we now have to find solutions for the electric potentials $U_{0,0}$, $U_{0,1}$, and $U_{2,0}$ and the drop interfaces $R_{2,0}$, $R_{2,1}$, and $R_{4,0}$ numerically. Figure 11 shows the numerically calculated values of $\alpha_{2,0}$, $\alpha_{2,1}$, and $\alpha_{4,0}$ plotted as functions of the cell gap D . As expected, for sufficiently large values of D , we recover the previously obtained constant values in the case of an infinite cell gap given by (50), but for smaller values of D , they deviate significantly from these values. In particular, we conclude that, in agreement with what we found from the numerical solutions of the theoretical model in Sec. IV, the infinite cell gap approximation is valid for $D \gtrsim 3$.

VI. SUMMARY AND DISCUSSION

In the present work, we have considered, both theoretically and experimentally, the deformation due to an electric field of a pinned nearly hemispherical static sessile drop of an ionic fluid with a high conductivity, resting on the lower substrate of a parallel-plate capacitor.

Numerical solutions of the theoretical model were found to agree very well with the experimental results. In addition, numerical solutions using two additional simplifying assumptions of negligible gravity, $G = 0$, and an infinite cell gap, $D \rightarrow \infty$, were also compared with the experimental results. For many of the 23 experiments, these two additional simplifying assumptions were valid, and so they were used to construct an asymptotic solution of the theoretical model in the limit of small electric Bond number, $\delta^2 \rightarrow 0$, and small deviations in the zero-field contact angles from $\pi/2$, $\epsilon \rightarrow 0$. This asymptotic solution for the drop interface extends that of Basaran and Scriven,¹⁸ and provides useful predictive equations for the changes in the height of the drop apex Δh , the contact angle $\Delta\theta_c$, and the modified pressure ΔP as functions of the zero-field contact angle θ_c , the drop width b_0 , the surface tension γ , and the applied electric field V/d .

The asymptotic solution required some numerical computations, and so an approximate analytical asymptotic solution was constructed which satisfies all of the conditions except the boundary condition on the lower substrate. The approximate asymptotic solutions for the change in the height of the drop apex Δh and the change in the contact angle $\Delta\theta_c$ agree surprisingly well with the full solution, although the approximate asymptotic solution for the change in the modified pressure ΔP is in less good agreement. As well as providing predictive equations for Δh , $\Delta\theta_c$, and ΔP , the approximate asymptotic solution also provides an analytical expression for the entire drop profile. The dimensional versions of both the asymptotic and the approximate analytical asymptotic solutions could have applications in material parameter estimation, particularly to obtain an estimate for the surface tension γ .

Our approach in this paper may be extended to similar systems, such as the geometry used to produce voltage-programmable microlenses.⁴¹ In this geometry, the fluid fills the region between

the electrodes and the upper electrode has an array of aperture holes through which the fluid protrudes, forming spherical and aspherical microlenses with pinned contact lines. In addition, future theoretical and experimental work will consider the dynamic response of a sessile drop immediately after the abrupt application and the abrupt removal of a voltage.

ACKNOWLEDGMENTS

This work was funded by the United Kingdom Engineering and Physical Sciences Research Council (EPSRC) via Research Grants EP/J009865 (Nottingham Trent University) and EP/J009873 (University of Strathclyde). SKW is also supported by Leverhulme Trust Research Fellowship RF-2013-355.

APPENDIX: ASYMPTOTIC SOLUTION FOR A FIXED CONTACT ANGLE

In this Appendix, we repeat the asymptotic analysis of Sec. V, but for a drop with a fixed contact angle rather than a pinned contact line. The solution process goes through exactly as before, except that the boundary condition for a pinned contact line (17) is replaced by the fixed contact angle condition

$$R'(\pi/2) = \cot \theta_c. \quad (\text{A1})$$

Recall that we write the zero-field contact angle as $\theta_c = \pi/2 - \epsilon$, so that in the limit $\epsilon \rightarrow 0$, this boundary condition becomes

$$R'(\pi/2) = \epsilon + \frac{\epsilon^3}{3} + O(\epsilon^5). \quad (\text{A2})$$

As before, we first find the asymptotic solution before finding an approximate analytical asymptotic solution in which the potential $U_{0,1}$ (but not in this case $U_{2,0}$, which we can obtain exactly) does not satisfy the boundary condition on the lower substrate.

1. Asymptotic solution

Considering each order of the normal stress balance (13) in turn, we find at $O(1)$ that $P_{0,0} = 2$, while at $O(\epsilon)$, $P_{0,1} = 0$. At $O(\delta^2)$, we obtain

$$R''_{2,0}(\theta) + \cot \theta R'_{2,0}(\theta) + 2R_{2,0}(\theta) = -P_{2,0} - \frac{9}{2} \cos^2 \theta, \quad (\text{A3})$$

where we have substituted in the leading order solution for the potential given by (35). Equation (A3) must be solved subject to the boundary conditions $R'_{2,0}(\pi/2) = 0$, $R'_{2,0}(0) = 0$, and the volume constraint (34), which gives the solutions

$$R_{2,0}(\theta) = \frac{3}{8} (3 \cos^2 \theta - 1) \quad (\text{A4})$$

and $P_{2,0} = -3/2$, recovering the leading order solution for a fixed contact angle found by Basaran and Scriven.¹⁸

At $O(\epsilon^2)$, we find that $P_{0,2} = -1$, while at $O(\delta^2\epsilon)$, we obtain

$$R''_{2,1}(\theta) + \cot \theta R'_{2,1}(\theta) + 2R_{2,1}(\theta) = -P_{2,1} - 3 \cos \theta U_{0,1r}|_{r=1} - \frac{9}{2} \cos \theta (\cos^2 \theta + 1), \quad (\text{A5})$$

subject to the boundary conditions $R'_{2,1}(\pi/2) = 0$, $R'_{2,1}(0) = 0$, and the volume constraint

$$\int_0^{\pi/2} R_{2,1} \sin \theta \, d\theta = \frac{3}{16}. \quad (\text{A6})$$

Furthermore, at $O(\delta^4)$, we obtain

$$R_{4,0}''(\theta) + \cot \theta R_{4,0}'(\theta) + 2R_{4,0}(\theta) = -P_{4,0} - 3 \cos \theta U_{2,0r}|_{r=1} + \frac{9}{32} (3 \cos^2 \theta - 1)(9 \cos^2 \theta + 5), \quad (\text{A7})$$

subject to the boundary conditions $R_{4,0}'(\pi/2) = 0$, $R_{4,0}'(0) = 0$, and the volume constraint

$$\int_0^{\pi/2} R_{4,0} \sin \theta \, d\theta = -\frac{9}{80}. \quad (\text{A8})$$

As in the pinned contact line case, to find $R_{2,1}$ and $R_{4,0}$, we need first to find $U_{0,1}$ and $U_{2,0}$. At $O(\epsilon)$, the system of equations governing $U_{0,1}$ is identical to the pinned contact line case (41)–(44), while at $O(\delta^2)$, the electric potential satisfies

$$\nabla^2 U_{2,0} = 0, \quad (\text{A9})$$

subject to the boundary and far-field conditions

$$U_{2,0}(r, \pi/2) = 0, \quad (\text{A10})$$

$$U_{2,0}(1, \theta) = -\frac{9}{8} \cos \theta (3 \cos^2 \theta - 1), \quad (\text{A11})$$

$$U_{2,0}(r, \theta) \rightarrow 0 \quad \text{as } r \rightarrow \infty. \quad (\text{A12})$$

Note that the $O(\delta^4)$ problem for $U_{2,0}$ differs only in the boundary condition on the drop interface (A11) (cf. (47)).

The system of Eqs. (41)–(44) is solved numerically as in the pinned contact line case. This solution is then used to solve (A5) numerically to obtain $P_{2,1}$ and $R_{2,1}(\theta)$. We find $P_{2,1} = 0.74973$, and the circles in Figure 12(a) show the solution for $R_{2,1}(\theta)$ plotted as a function of θ/π . In contrast to the pinned contact line case, the system of Eqs. (A9)–(A12) governing $U_{2,0}$ is separable and has the exact analytical solution

$$U_{2,0} = -\frac{9}{40} \left(\frac{4 \cos \theta}{r^2} + \frac{3(5 \cos^3 \theta - 3 \cos \theta)}{r^4} \right). \quad (\text{A13})$$

Substituting this solution for $U_{2,0}$ into the equation for $R_{4,0}(\theta)$, (A7), gives

$$R_{4,0}''(\theta) + \cot \theta R_{4,0}'(\theta) + 2R_{4,0}(\theta) = -P_{4,0} - \frac{1053}{32} \cos^4 \theta + \frac{1647}{80} \cos^2 \theta - \frac{45}{32}, \quad (\text{A14})$$

subject to the boundary conditions $R_{4,0}'(\pi/2) = 0$, $R_{4,0}'(0) = 0$, and the volume constraint (A8), which has solutions

$$R_{4,0}(\theta) = \frac{117}{64} \cos^4 \theta + \frac{27}{80} \cos^2 \theta - \frac{189}{320} \quad (\text{A15})$$

and $P_{4,0} = -9/10$. Figure 12(b) shows the solution for $R_{4,0}(\theta)$ plotted as a function of θ/π .

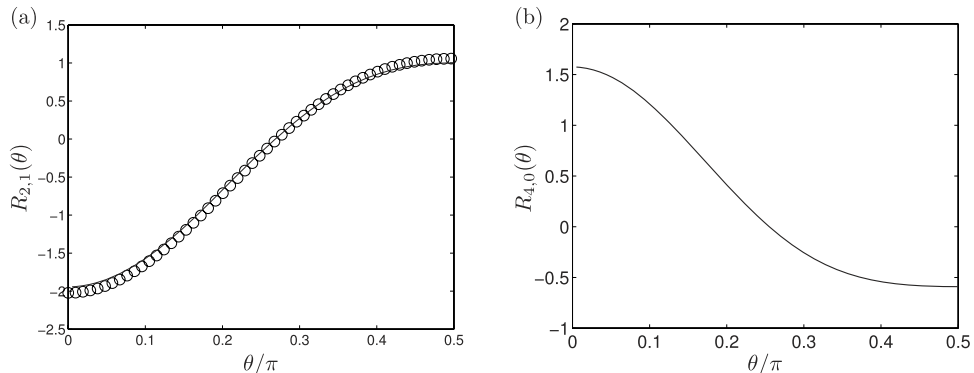


FIG. 12. (a) The full numerical solution (shown with circles) and the approximate solution (shown with a solid line) for $R_{2,1}(\theta)$ and (b) the exact analytical solution for $R_{4,0}(\theta)$ plotted as functions of θ/π .

At the drop apex, we find that

$$R(0) = 1 - \epsilon + \frac{3}{4}\delta^2 + \frac{1}{2}\epsilon^2 - 2.02278\delta^2\epsilon + \frac{63}{40}\delta^4 + O(\epsilon^3, \delta^2\epsilon^2, \delta^4\epsilon, \delta^6), \quad (\text{A16})$$

and hence the change in the height of the drop apex Δh is given by

$$\Delta h = \frac{3}{4}\delta^2 - 2.02278\delta^2\epsilon + \frac{63}{40}\delta^4 + O(\delta^2\epsilon^2, \delta^4\epsilon, \delta^6). \quad (\text{A17})$$

In this case, instead of a change in the contact angle $\Delta\theta_c$, we have a change in the radius Δb which is given by

$$\begin{aligned} \Delta b &= R(\pi/2) - R(\pi/2)|_{\delta^2=0} \\ &= -\frac{3}{8}\delta^2 + 1.05732\delta^2\epsilon - \frac{189}{320}\delta^4 + O(\delta^2\epsilon^2, \delta^4\epsilon, \delta^6), \end{aligned} \quad (\text{A18})$$

and the change in the modified pressure ΔP is given by

$$\Delta P = -\frac{3}{2}\delta^2 + 0.74973\delta^2\epsilon - \frac{9}{10}\delta^4 + O(\delta^2\epsilon^2, \delta^4\epsilon, \delta^6). \quad (\text{A19})$$

2. Approximate asymptotic solution

Proceeding as in Sec. V B, we find that the separable part for $U_{0,1}^s$ is given by (53). Substituting this into Eq. (A5) gives

$$R_{2,1}''(\theta) + \cot\theta R_{2,1}'(\theta) + 2R_{2,1}(\theta) = -P_{2,1} + \frac{3}{2}\cos\theta(15\cos^2\theta - 7), \quad (\text{A20})$$

subject to the boundary conditions $R_{2,1}'(\pi/2) = 0$, $R_{2,1}'(0) = 0$, and the volume constraint (A6), which has solutions

$$R_{2,1}(\theta) = 1 - \frac{9}{4}\cos^3\theta - \cos\theta \ln(1 + \cos\theta) \quad (\text{A21})$$

and $P_{2,1} = 0$. Figure 12(a) compares the approximate solution (A21) (shown with a solid line) with the corresponding full numerical solution for $R_{2,1}(\theta)$ (shown with circles). There is surprisingly good agreement between the two solutions even close to the lower substrate at $\theta = \pi/2$, even though the right-hand side of (55) is determined by the separable solution which does not satisfy the boundary condition there.

From these approximate solutions, the corresponding approximate asymptotic solution for the change in the height of the drop apex Δh is given by

$$\begin{aligned} \Delta h &= \frac{3}{4}\delta^2 - \left(\frac{5}{4} + \ln 2\right)\delta^2\epsilon + \frac{63}{40}\delta^4 + O(\delta^2\epsilon^2, \delta^4\epsilon, \delta^6) \\ &= \frac{3}{4}\delta^2 - 1.9431\delta^2\epsilon + \frac{63}{40}\delta^4 + O(\delta^2\epsilon^2, \delta^4\epsilon, \delta^6), \end{aligned} \quad (\text{A22})$$

the change in the radius Δb is given by

$$\Delta b = -\frac{3}{8}\delta^2 + \delta^2\epsilon - \frac{189}{320}\delta^4 + O(\delta^2\epsilon^2, \delta^4\epsilon, \delta^6), \quad (\text{A23})$$

and the change in the modified pressure ΔP is given by

$$\Delta P = -\frac{3}{2}\delta^2 - \frac{9}{10}\delta^4 + O(\delta^2\epsilon^2, \delta^4\epsilon, \delta^6). \quad (\text{A24})$$

Comparing these approximate asymptotic results (A22)–(A24) with the asymptotic results given by (A17)–(A19), we see that the approximate solutions for Δh and Δb agree very well with the full solution, but again the approximate solution for ΔP is in less good agreement.

- ¹ R. A. Millikan, "On the elementary electrical charge and the Avogadro constant," *Phys. Rev.* **2**, 109–143 (1913).
- ² J. C. Baygents and D. A. Saville, "Electrophoresis of drops and bubbles," *J. Chem. Soc., Faraday Trans.* **87**, 1883–1898 (1991).
- ³ D. J. Im, J. Noh, D. Moon, and I. Kang, "Electrophoresis of a charged droplet in a dielectric liquid for droplet actuation," *Anal. Chem.* **83**, 5168–5174 (2011).
- ⁴ F. Mugele, M. Duits, and D. van den Ende, "Electrowetting: A versatile tool for drop manipulation, generation, and characterization," *Adv. Colloid Interface Sci.* **161**, 115–123 (2005).
- ⁵ M. G. Pollack, R. B. Fair, and A. Shenderov, "Electrowetting-based actuation of liquid droplets for microfluidic applications," *Appl. Phys. Lett.* **77**, 1725–1726 (2000).
- ⁶ R. B. Fair, "Digital microfluidics: Is a true lab-on-a-chip possible?," *Microfluid. Nanofluid.* **3**, 245–281 (2007).
- ⁷ H. A. Pohl, *Dielectrophoresis: The Behaviour of Neutral Matter in Non-Uniform Electric Fields* (Cambridge University Press, 1978).
- ⁸ R. Pethig, "Dielectrophoresis: Status of the theory, technology, and applications," *Biomicrofluidics* **4**, 022811 (2010).
- ⁹ L. D. Landau and E. M. Lifshitz, *The Classical Theory of Fields*, 6th ed. (Elsevier, 1987).
- ¹⁰ K. H. Kang, "How electrostatic fields change contact angle in electrowetting," *Langmuir* **18**, 10318–10322 (2002).
- ¹¹ L. Y. Yeo and H.-C. Chang, "Static and spontaneous electrowetting," *Mod. Phys. Lett. B* **19**, 549–569 (2005).
- ¹² T. B. Jones, "Liquid dielectrophoresis on the microscale," *J. Electrostat.* **51–52**, 290–299 (2001).
- ¹³ K. L. Wang, T. B. Jones, and A. Raisanen, "DEP actuated nanoliter droplet dispensing using feedback control," *Lab Chip* **9**, 901–909 (2009).
- ¹⁴ C. V. Brown, G. G. Wells, M. I. Newton, and G. McHale, "Voltage-programmable liquid optical interface," *Nat. Photonics* **3**, 403–405 (2009).
- ¹⁵ A. Klingner, S. Herminghaus, and F. Mugele, "Self-excited oscillatory dynamics of capillary bridges in electric fields," *Appl. Phys. Lett.* **82**, 4187–4189 (2003).
- ¹⁶ A. Klingner, J. Buehrle, and F. Mugele, "Capillary bridges in electric fields," *Langmuir* **20**, 6770–6777 (2004).
- ¹⁷ G. I. Taylor, "Disintegration of water drops in an electric field," *Proc. R. Soc. London A* **280**, 383–397 (1964).
- ¹⁸ O. A. Basaran and L. E. Scriven, "Axisymmetric shapes and stability of pendant and sessile drops in an electric field," *J. Colloid Interface Sci.* **140**, 10–30 (1990).
- ¹⁹ S. N. Reznik, A. L. Yarin, A. Theron, and E. Zussman, "Transient and steady shapes of droplets attached to a surface in a strong electric field," *J. Fluid Mech.* **516**, 349–377 (2004).
- ²⁰ C. Roero, "Contact-Angle Measurements of Sessile Drops Deformed by a DC Electric Field," in *Contact Angle, Wettability and Adhesion*, edited by K. L. Mittal (CRC Press, Taylor and Francis Group, Boca Raton, FL, USA, 2006), Vol. 4, pp. 165–176.
- ²¹ A. Bateni, S. Susnar, A. Amirfazli, and A. Neumann, "Development of a new methodology to study drop shape and surface tension in electric fields," *Langmuir* **20**, 7589–7597 (2004).
- ²² A. Bateni, A. Ababneh, J. A. W. Elliott, A. Neumann, and A. Amirfazli, "Effect of gravity and electric field on shape and surface tension of drops," *Adv. Space Res.* **36**, 64–69 (2005).
- ²³ J. M. Roux, J. L. Achard, and Y. Fouillet, "Forces and charges on an undeformable droplet in the DC field of a plate condenser," *J. Electrostat.* **66**, 283–293 (2008).
- ²⁴ A. Bateni, S. Laughton, H. Tavana, S. Susnar, A. Amirfazli, and A. Neumann, "Effect of electric fields on contact angle and surface tension of drops," *J. Colloid Interface Sci.* **283**, 215–222 (2005).
- ²⁵ A. Bateni, A. Amirfazli, and A. Neumann, "Effects of an electric field on the surface tension of conducting drops," *Colloids Surf., A* **289**, 25–38 (2006).
- ²⁶ C. Tsakonas, L. Corson, I. C. Sage, and C. V. Brown, "Electric field induced deformation of hemispherical sessile drops of ionic liquid," *J. Electrostat.* **72**, 437–440 (2014).
- ²⁷ V. Vancauwenberghe, P. Di Marco, and D. Brutin, "Wetting and evaporation of a sessile drop under an external electric field: A review," *Colloids Surf., A* **432**, 50–56 (2013).
- ²⁸ F. K. Wohlhuter and O. A. Basaran, "Shapes and stability of pendant and sessile dielectric drops in an electric field," *J. Fluid Mech.* **235**, 481–510 (1992).
- ²⁹ O. A. Basaran and F. K. Wohlhuter, "Effect of nonlinear polarization on shapes and stability of pendant and sessile drops in an electric (magnetic) field," *J. Fluid Mech.* **244**, 1–16 (1992).
- ³⁰ C. Ferrera, J. M. López-Herrera, M. A. Herrada, J. M. Montanero, and A. J. Acero, "Dynamical behavior of electrified pendant drops," *Phys. Fluids* **25**, 012104 (2013).
- ³¹ Y.-H. Yu, A. N. Soriano, and M.-H. Li, "Heat capacity and electrical conductivity of aqueous mixtures of [Bmim][BF₄] and [Bmim][PF₆]," *J. Taiwan Inst. Chem. Eng.* **40**, 205–212 (2009).
- ³² Y. Chauvin, L. Mussmann, and H. Olivier, "A novel class of versatile solvents for two-phase catalysis: Hydrogenation, isomerization, and hydroformylation of alkenes catalysed by rhodium complexes in liquid 1,3-dialkylimidazolium salts," *Angew. Chem., Int. Ed. Engl.* **34**, 2698–2700 (1995).
- ³³ P. A. Z. Suarez, J. E. L. Dullins, S. Einloft, R. F. D. Souza, and J. Dupont, "The use of new ionic liquids in two-phase catalytic hydrogenation reaction by rhodium complexes," *Polyhedron* **15**, 1217–1219 (1996).
- ³⁴ Z. Fei and P. J. Dyson, "The making of iLiquids - the chemist's equivalent of the iPhone," *Chem. Commun.* **49**, 2594–2596 (2013).
- ³⁵ A. W. Adamson and A. P. Gast, *Physical Chemistry of Surfaces*, 4th ed. (John Wiley & Sons, Inc., 1997).

- ³⁶ J. G. Huddleston, A. E. Visser, W. M. Reichert, H. Willauer, G. A. Broker, and R. D. Rogers, "Characterization and comparison of hydrophilic and hydrophobic room temperature ionic liquids incorporating the imidazolium cation," *Green Chem.* **3**, 156–164 (2001).
- ³⁷ MATLAB, *version 8.1, R2013a*, The MathWorks, Inc., Natick, Massachusetts, 2013.
- ³⁸ The charge relaxation time of BMIMTfB can be estimated from literature values of its conductivity³¹ σ and its relative permittivity at room temperature³⁹ $\epsilon_1 = \epsilon_{\text{fluid}}/\epsilon_0$, where ϵ_0 is the permittivity of free space, to be of the order of $\epsilon_0\epsilon_1/\sigma \approx 10^{-5} - 10^{-6} \text{ s}^{-1}$, which is small compared to the reciprocal of the frequency of the field, 10^{-3} s^{-1} .
- ³⁹ J. Sangoro, C. Iacob, A. Serghei, S. Naumov, P. Galvosas, J. Kärger, C. Wespe, F. Bordusa, A. Stoppa, J. Hunger, R. Buchner, and F. Kremer, "Electrical conductivity and translational diffusion in the 1-butyl-3-methylimidazolium tetrafluoroborate ionic liquid," *J. Chem. Phys.* **128**, 214509 (2008).
- ⁴⁰ COMSOL Multiphysics, *version 4.3b*, COMSOL, Inc., 2013.
- ⁴¹ C. U. Murade, D. van der Ende, and F. Mugele, "High speed adaptive liquid microlens array," *Opt. Express* **20**, 18180–18187 (2012).